Available online at www.sciencedirect.com
ScienceDirect
International Journal of Heat and Mass Transfer 51 (2008) 1156–1167
International Journal of HEAT and MASS TRANSFER
www.elsevier.com/locate/ijhmt

Three-dimensional simulation of saturated film boiling on a horizontal cylinder

Gihun Son [a], Vijay K. Dhir [b,*]

[a] Department of Mechanical Engineering, Sogang University, Seoul 121–742, South Korea
[b] Mechanical and Aerospace Engineering Department, University of California, Los Angeles, CA 90095, USA

Received 17 November 2006; received in revised form 10 April 2007
Available online 12 July 2007

Abstract

Three-dimensional simulations of film boiling on a horizontal cylinder have been performed. A finite difference method is used to solve the equations governing the conservation of mass, momentum and energy in vapor and liquid phases. A level set formulation for tracking the liquid–vapor interface is modified to include the effect of phase change at the liquid–vapor interface and to treat the no-slip condition at the fluid–solid interface. From the numerical simulations, the effects of cylinder diameter and gravity on the interfacial motion and heat transfer in film boiling are quantified. The heat transfer coefficients obtained from numerical analysis are found to compare well with those predicted from empirical correlations reported in the literature.

Keywords: Film boiling; Immersed solid boundary; Level set method; Numerical simulation

1. Introduction

In film boiling on a horizontal cylinder, a continuous vapor layer forms between the heated cylinder and the surrounding liquid. The vapor is generated at the liquid–vapor interface of the thin film region on the lower portion of the cylinder and is removed on the upper portion through the formation and release of bubbles, which is determined by Taylor instability.

Bromley [1] first presented a theoretical model for saturated film boiling on a horizontal cylinder. Using boundary-layer approximations, he predicted Nusselt number for film boiling as

$$Nu_B = 0.62[GrPr_v/(1 + 0.34Ja)]^{1/4} \quad (1)$$

where the lead constant was adjusted from experimental data. This prediction based on boundary-layer analysis is valid only when the cylinder diameter is much larger in comparison to the vapor film thickness.

While experimentally studying the effect of cylinder diameter on film boiling, Breen and Westwater [2] found that Bromley's equation (1) did not work when the cylinder diameter, D, was very small or larger than the most unstable (or dangerous) Taylor wavelength for a flat plate, λ_{dF} ($= 2\pi\sqrt{3}l_0$, where $l_0 = \sqrt{\sigma/g(\rho_l - \rho_v)}$). This observation implies that the heat transfer mechanism in film boiling on a cylinder is affected by the pattern of interfacial waves. Including the effect of surface tension, Breen and Westwater proposed an empirical correlation for a wide range of cylinder diameters

$$Nu = (0.601\widehat{D}^{1/4} + 0.442/\widehat{D}^{3/4})Nu_B \quad (2)$$

where $\widehat{D} = D/l_0$.

Sakurai et al. [3] proposed a more comprehensive correlation for predicting the heat transfer coefficient for saturated and subcooled film boiling on horizontal cylinders. Modifying an approximate solution for the vapor as well as liquid boundary layers, they developed a semi-empirical

* Corresponding author. Present address: 7400 Boelter Hall, 420 Westwood Plaza, University of California, Los Angeles, CA 90095, USA. Tel.: +1 310 825 8507; fax: +1 310 206 2302.
E-mail address: vdhir@seas.ucla.edu (V.K. Dhir).

0017-9310/$ - see front matter © 2007 Published by Elsevier Ltd.
doi:10.1016/j.ijheatmasstransfer.2007.04.026

Nomenclature

c	specific heat
D	cylinder diameter
$\widehat{D}$	dimensionless cylinder diameter, D/l_0
$\widehat{D}_I$	dimensionless diameter of the cylindrical interface
F	fraction function
g	gravity
Gr	Grashof number, $\rho_v(\rho_l-\rho_v)gD^3/\mu_v^2$
h	grid spacing
h_{lv}	latent heat of vaporization
H	discontinuous step function
Ja	Jakob number, $c_v(T_w-T_{sat})/h_{lv}$
k	thermal conductivity
l_0	reference length, $\sqrt{\sigma/g(\rho_l-\rho_v)}$
$\dot{m}$	mass flux across the interface
$\mathbf{n}$	unit normal vector
Nu	Nusselt number, $Dq_w/k_v(T_w-T_{sat})$
Nu_B	Nusselt number predicted from Bromley's correlation
P	pressure
Pr	Prandtl number, $\mu c/k$
q_w	wall heat flux
S	sign function
t	time
t_0	reference time, $\sqrt{l_0/g}$
$\mathbf{u}$	velocity vector
$\mathbf{U}$	interface velocity vector
x, y, z	Cartesian coordinates

Greek symbols

α	$\rho_v^{-1}-\rho_l^{-1}$
κ	interface curvature
λ	wavelength
λ_c	critical wavelength
λ_d	most dangerous wavelength
μ	dynamic viscosity
ρ	density
σ	surface tension coefficient
τ	artificial time
ϕ	distance function from the liquid–vapor interface
ψ	distance function from the fluid–solid interface

Subscripts

e	earth
f	liquid or vapor
F	flat plate
I	interface
l,v	liquid, vapor
sat	saturation
w	solid

correlation for film boiling which covered a broad range of fluid properties, cylinder diameters, wall superheats, liquid subcoolings and system pressures. For saturated film boiling, the correlation is reduced to

$$\frac{Nu}{1+2/Nu}=C_s[0.919-0.0287(\ln\widehat{D})+0.0578(\ln\widehat{D})^2]Nu_B \tag{3}$$

where C_S is a function of $\rho_v\mu_v/\rho_l\mu_l$, a/Pr_v and Pr_l.

While developing a prediction model for heat transfer in film boiling, Nishio and Ohtake [4] described the vapor layer around the cylinder as a series of two-dimensional vapor-film-units. Each unit (or cell) consists of a thin vapor film, in which most of vapor generation occurs, and a vapor dome which absorbs the vapor. They assumed that the length of each unit is determined by the Kelvin–Helmholtz instability and the development of vapor layer along the perimeter of a horizontal cylinder is not continued beyond the vapor-film-unit length. This model is effective for cylinders in a large-diameter region, whose perimeter is much longer than the vapor-film-unit length.

A theoretical model for describing Taylor waves in film boiling on a horizontal cylinder was developed by Lienhard and Wong [5]. Adding the transverse component of surface tension, which was evaluated from a simply assumed cylindrical interface configuration, they derived an expression for the most dangerous wavelength on a horizontal cylinder as

$$\lambda_d=\lambda_{dF}/\sqrt{1+2/\widehat{D}^2} \tag{4}$$

Replacing the cylinder diameter, $\widehat{D}$, with the actual diameter of the cylindrical interface, $\widehat{D}_I$, Lienhard and Sun [6] modified Eq. (4) as

$$\lambda_d=\lambda_{dF}/\sqrt{1+2/\widehat{D}_I^2} \tag{5}$$

They evaluated $\widehat{D}_I$ using a simple model equation for the vapor film thickness. The experimentally observed wavelengths were found to lie in the range of +60% and −25% of those predicted from Eq. (5).

Recently, numerical simulations for directly analyzing the interfacial motion and heat transfer in film boiling have been performed in several studies. For computations of film boiling on a horizontal flat plate, Son and Dhir [7] used a moving-grid method, in which the matching conditions at the interface can be imposed accurately. Juric and Tryggvason [8] employed a front-tracking method, in which the interface is represented explicitly by the linked line or surface elements. Generally the Lagrangian methods are not straightforward for implementation of the interface with change in topology. To overcome such difficulties, Son and Dhir [9] adopted the level set method, in which

the interface is tracked by a smooth distance function, and Welch and Wilson [10] used the volume-of-fluid method, which tracks the volume fraction of a particular phase rather than the interface itself.

Only a few computations have been made for film boiling on a horizontal cylinder because of the complexities in treatment of an immersed solid surface. Very recently, Esmaeeli and Tryggvason [11] have extended the front-tracking method to film boiling on horizontal cylinders while combining with an immersed boundary method [12] to account for the velocity boundary conditions on irregular solid surfaces. They have demonstrated a three-dimensional evolution pattern of the liquid–vapor interface including the formation and pinch-off of a bubble. However, their prediction for heat transfer coefficient is based on two-dimensional computations, which can not capture the interfacial wave motion appropriately, and the predicted values are quite different from those obtained from correlations derived from experimental data.

In this study, complete numerical simulations of film boiling on a horizontal cylinder are performed for a detailed analysis of three-dimensional characteristics of interfacial motion and for a general prediction of the associated heat transfer without employing any empirical data. The effects of cylinder diameter and gravity on the interfacial motion and heat transfer are investigated through the direct numerical simulations.

2. Numerical analysis

For numerically simulating film boiling on a horizontal cylinder, the level set (LS) formulation modified by Son and Dhir [13] to include the effect of phase change at the liquid–vapor interface and to treat the no-slip condition at the fluid–solid interface is used. The liquid–vapor interface is tracked by a LS function, ϕ, which is defined as a signed distance from the interface. The negative sign is chosen for the vapor phase and the positive sign for the liquid phase.

The equations governing the conservation of mass, momentum and energy for each phase are written as

$$\nabla \cdot \mathbf{u}_{\mathrm{f}} = 0 \tag{6}$$

$$\rho_{\mathrm{f}}\left(\frac{\partial \mathbf{u}_{\mathrm{f}}}{\partial t} + \mathbf{u}_{\mathrm{f}} \cdot \nabla \mathbf{u}_{\mathrm{f}}\right) = -(\nabla p)_{\mathrm{f}} + \rho_{\mathrm{f}}\mathbf{g} + \nabla \cdot \mu_{\mathrm{f}}(\nabla \mathbf{u} + \nabla \mathbf{u}^{\mathrm{T}})_{\mathrm{f}} \tag{7}$$

$$\rho_{\mathrm{f}} c_{\mathrm{f}}\left(\frac{\partial T_{\mathrm{f}}}{\partial t} + \mathbf{u}_{\mathrm{f}} \cdot \nabla T_{\mathrm{f}}\right) = \nabla \cdot k_{\mathrm{f}}(\nabla T)_{\mathrm{f}} \tag{8}$$

where the subscript "f" denotes the liquid phase for $\phi > 0$ and the vapor phase for $\phi < 0$. The conservation equations for each phase are coupled through the matching (or jump) conditions at the interface:

$$\mathbf{u}_{\mathrm{l}} - \mathbf{u}_{\mathrm{v}} = \alpha \dot{m}\mathbf{n} \tag{9}$$

$$\mathbf{n} \cdot [\mu_{\mathrm{l}}(\nabla \mathbf{u} + \nabla \mathbf{u}^{\mathrm{T}})_{\mathrm{l}} - \mu_{\mathrm{v}}(\nabla \mathbf{u} + \nabla \mathbf{u}^{\mathrm{T}})_{\mathrm{v}}] \times \mathbf{n} = 0 \tag{10}$$

$$-p_{\mathrm{l}} + p_{\mathrm{v}} + \mathbf{n} \cdot [\mu_{\mathrm{l}}(\nabla \mathbf{u} + \nabla \mathbf{u}^{\mathrm{T}})_{\mathrm{l}} - \mu_{\mathrm{v}}(\nabla \mathbf{u} + \nabla \mathbf{u}^{\mathrm{T}})_{\mathrm{v}}] \cdot \mathbf{n} = \sigma\kappa - \alpha \dot{m}^2 \tag{11}$$

where $\alpha = \rho_{\mathrm{v}}^{-1} - \rho_{\mathrm{l}}^{-1}$. The normal, $\mathbf{n}$, to the interface, the interface curvature, κ, and the mass flux, $\dot{m}$, are defined as

$$\mathbf{n} = \nabla\phi/|\nabla\phi| \tag{12}$$

$$\kappa = \nabla \cdot \mathbf{n} \tag{13}$$

$$\dot{m} = \rho_{\mathrm{f}}(\mathbf{U} - \mathbf{u}_{\mathrm{f}}) \cdot \mathbf{n} \tag{14}$$

where $\mathbf{U}$ is the interface velocity. The interface temperature is specified as a Dirichlet boundary condition, $T_{\mathrm{f}} = T_{\mathrm{sat}}$. The mass flux $\dot{m}$ is evaluated from the energy balance at the interface

$$\dot{m} = \frac{1}{h_{\mathrm{lv}}}\mathbf{n} \cdot (k_{\mathrm{l}}\nabla T_{\mathrm{l}} - k_{\mathrm{v}}\nabla T_{\mathrm{v}}) \tag{15}$$

For its efficient implementation, $\dot{m}$ is extrapolated into the entire domain (or a narrow band near the interface) by the calculation procedure developed in [14].

Based on the ghost fluid approach [14–19], which is a numerical technique for accurately enforcing the boundary or matching conditions at the interface without being smoothed over several grid spacings, the conservation equations can be rewritten for the liquid–vapor region as

$$\nabla \cdot \mathbf{u} = \alpha \dot{m}\mathbf{n} \cdot \nabla H_{\phi} \tag{16}$$

$$\hat{\rho}\left(\frac{\partial \mathbf{u}}{\partial t} + \mathbf{u}_{\mathrm{f}} \cdot \nabla \mathbf{u}_{\mathrm{f}}\right) = -[\nabla p + (\sigma\kappa - \alpha \dot{m}^2)\nabla H_{\phi}] + \hat{\rho}\mathbf{g} + \nabla \cdot \hat{\mu}(\nabla \mathbf{u} + \nabla \mathbf{u}^{\mathrm{T}}) - \nabla \cdot \hat{\mu}[(\alpha \dot{m}\mathbf{n}\nabla H_{\phi})^{\mathrm{T}} + \alpha \dot{m}\mathbf{n}\nabla H_{\phi}] \tag{17}$$

$$\rho_{\mathrm{f}} c_{\mathrm{f}}\left(\frac{\partial T_{\mathrm{f}}}{\partial t} + \mathbf{u}_{\mathrm{f}} \cdot \nabla T_{\mathrm{f}}\right) = \nabla \cdot \hat{k}_{\mathrm{f}}\nabla T_{\mathrm{f}} \quad \text{if } \phi \neq 0$$

$$T_{\mathrm{f}} = 0 \quad \text{if } \phi = 0 \tag{18}$$

where

$$H_{\phi} = \begin{cases} 1 & \text{if } \phi > 0 \\ 0 & \text{if } \phi \leqslant 0 \end{cases}$$

$$\mathbf{u}_{\mathrm{l}} = \mathbf{u} + \alpha \dot{m}\mathbf{n}(1 - H_{\phi})$$

$$\mathbf{u}_{\mathrm{v}} = \mathbf{u} - \alpha \dot{m}\mathbf{n}H_{\phi}$$

$$\hat{\rho} = \rho_{\mathrm{v}}(1 - F_{\phi}) + \rho_{\mathrm{l}}F_{\phi}$$

$$\hat{\mu}^{-1} = \mu_{\mathrm{v}}^{-1}(1 - F_{\phi}) + \mu_{\mathrm{l}}^{-1}F_{\phi}$$

$$\hat{k}_{\mathrm{f}} = \begin{cases} \hat{k}_{\mathrm{l}} = k_{\mathrm{l}}/F_{\phi} & \text{if } \phi > 0 \\ \hat{k}_{\mathrm{v}} = k_{\mathrm{v}}/(1 - F_{\phi}) & \text{if } \phi < 0 \end{cases}$$

Here, H is the discontinuous step function rather than the smoothed step function varying over several grid spacings and $\mathbf{u}_{\mathrm{f}}$ is the velocity for each phase which is extrapolated into the entire domain by using the velocity jump condition given by Eq. (9). The effective (or interpolated) properties,

($\hat{\rho}, \hat{\mu}$, and $\hat{k}_f$), are evaluated from a fraction function, F_ϕ, which is defined as

$$F_\phi = \begin{cases} 1 & \text{if } H(\phi_A) = H(\phi_B) = 1 \\ 0 & \text{if } H(\phi_A) = H(\phi_B) = 0 \\ \frac{\max(\phi_A,\phi_B)}{\max(\phi_A,\phi_B)-\min(\phi_A,\phi_B)} & \text{otherwise} \end{cases}$$

where ϕ_A and ϕ_B are obtained at the adjacent grid points [13]. Similar formulations for the effective properties have also been proposed by Sussman et al. [19].

In the LS formulation, the interface is described as $\phi = 0$. The zero level set of ϕ is advanced as

$$\frac{\partial \phi}{\partial t} + \mathbf{U} \cdot \nabla \phi = 0 \tag{19}$$

where $\mathbf{U}$ can be written from Eq. (14) as $\mathbf{U} = \mathbf{u}_f + \hat{m}\mathbf{n}/\rho_f$. The LS function is reinitialized to a distance function from the interface by obtaining a steady-state solution of the equation [20]

$$\frac{\partial \phi}{\partial \tau} = S(\phi_0)(1 - |\nabla \phi|) \tag{20}$$

where

$$S(\phi_0) = \begin{cases} 0 & \text{if } |\phi_0| \leqslant d_\epsilon \\ \frac{\phi_0}{\sqrt{\phi_0^2 + h^2}} & \text{otherwise} \end{cases}$$

Here h is a grid spacing, ϕ_0 is a solution of equation (19), and d_ϵ is the distance between the interface and the nearest grid point. The formulation given for the smoothed sign function S implies that a near-zero level set rather than $\phi = 0$ is used as the immobile boundary condition during the reinitialization procedure. This formulation of the sign function improves the LS method significantly [21].

To preserve mass conservation from any numerical errors occurring in numerical implementation of the LS advection and reinitialization procedures, the following volume-correction step is added to the level set formulation:

$$\frac{\partial \phi}{\partial \tau} = (V_v - V_{v0})|\nabla \phi| \tag{21}$$

where V_v is a vapor volume computed form ϕ and V_{v0} the vapor volume that satisfies mass conservation.

The governing equations are spatially discretized on a staggered grid system in which the velocity components are defined at cell faces whereas the other dependent variables at cell centers. A second-order ENO scheme is used for the convection terms and the distance function and a second-order central difference scheme for the other terms. While discretizing the governing equations temporally, the convection and source terms are treated by a first-order explicit scheme and the diffusion terms by a fully implicit scheme as follows:

$$\frac{\phi^{n+1} - \phi^n}{\Delta t} = -\mathbf{U}^n \cdot \nabla \phi^n \tag{22}$$

$$\frac{T_f^{n+1} - T_f^n}{\Delta t} = -\mathbf{u}_f^n \cdot \nabla T_f^n + \frac{1}{\rho_f c_f}(\nabla \cdot \hat{k}_f \nabla T_f^{n+1}) \tag{23}$$

$$\frac{\mathbf{u}^{n+1} - \mathbf{u}^*}{\Delta t} = -\frac{1}{\hat{\rho}}[\nabla p + (\sigma\kappa - \alpha \dot{m}^2)\nabla H_\phi] + \frac{1}{\hat{\rho}}(\nabla \cdot \hat{\mu} \nabla \mathbf{u}^{n+1} + \mathbf{s}_u) \tag{24}$$

$$\nabla \cdot \mathbf{u}^{n+1} = \alpha \dot{m} \mathbf{n} \cdot \nabla H_\phi \tag{25}$$

where

$$\mathbf{u}^* = \mathbf{u}_f^n + \Delta t(-\mathbf{u}_f^n \cdot \nabla \mathbf{u}_f^n + \mathbf{g})$$

$$\mathbf{s}_u = \nabla \cdot \hat{\mu}(\nabla \mathbf{u}^n)^T - \nabla \cdot \hat{\mu}[(\alpha \dot{m} \mathbf{n} \nabla H_\phi)^T + \alpha \dot{m} \mathbf{n} \nabla H_\phi]$$

Here, the effective properties and the step function are evaluated from ϕ^{n+1}, and $\dot{m}$ from T^{n+1}. The momentum equation (24) and the mass equation (25) are solved by employing the projection method [17]. We decompose Eq. (24) into two steps

$$\frac{\mathbf{u}^{**} - \mathbf{u}^*}{\Delta t} = \frac{1}{\hat{\rho}}(\nabla \cdot \hat{\mu} \nabla \mathbf{u}^{**} + \mathbf{s}_u) \tag{26}$$

$$\frac{\mathbf{u}^{n+1} - \mathbf{u}^{**}}{\Delta t} = -\frac{1}{\hat{\rho}}[\nabla p + (\sigma\kappa - \alpha \dot{m}^2)\nabla H_\phi] \tag{27}$$

In order to treat an immersed solid surface, we introduce another LS function, ψ, which is defined as a signed distance from the fluid–solid interface. The negative sign is chosen for the solid region and the positive sign for the fluid region. In this study, we assume that the solid is stationary and is maintained at a constant temperature, T_w. The energy conservation equation (18) is easily extended for this case by using a fraction function F_ψ for $\hat{k}_f$ near the solid surface as using F_ϕ near the liquid–vapor interface [13]. Also, the momentum Eqs. (26) and (27) can be extended for two-fluid flows with an immersed solid boundary condition as

$$\mathbf{u}^{**} = H_\psi \left[\mathbf{u}^* + \frac{\Delta t}{\hat{\rho}}(\nabla \cdot \hat{\mu} \nabla \mathbf{u}^{**} + \mathbf{s}_u) \right] \tag{28}$$

$$\mathbf{u}^{n+1} = \mathbf{u}^{**} - H_\psi \frac{\Delta t}{\hat{\rho}}[\nabla p + (\sigma\kappa - \alpha \dot{m}^2)\nabla H_\phi] \tag{29}$$

where $\hat{\hat{\mu}} = \hat{\mu}/F_\psi$. Substituting Eq. (29) into the mass conservation equation (25), the governing equation for pressure is obtained as

$$\nabla \cdot \frac{H_\psi}{\hat{\rho}} \nabla p = \frac{\nabla \cdot \mathbf{u}^{**} - (\alpha \dot{m} \mathbf{n} \cdot \nabla H_\phi)}{\Delta t} - \nabla \cdot \frac{H_\psi}{\hat{\rho}}(\sigma\kappa - \alpha \dot{m}^2)\nabla H_\phi \tag{30}$$

The present numerical method was tested in our previous study [13] through the computations of bubble rise in a stationary liquid, single-phase fluid flow past a circular cylinder and phase-change problems with immersed solid boundaries. The numerical results showed good agreement with the exact solutions or the numerical results available in the literature. Also, the convergence test for grid resolutions using different mesh sizes of $h = 0.02$, $h = 0.01$, and $h = 0.005$ was made for two-dimensional film boiling on a horizontal cylinder. As the grid spacing decreases, the relative difference of the Nusselt numbers between successive mesh sizes becomes small. For $h = 0.01$ and $h = 0.005$, the Nusselt number averaged over the computational period differed by less than 3%.

3. Results and discussion

Three-dimensional computations of film boiling were performed in a hexahedral domain including a horizontal cylinder located at $(x, y) = (0,0)$, as depicted in Fig. 1. The slip boundary condition is imposed at all of the computational boundaries except the top of the domain, which is treated as an open boundary. In carrying out numerical simulation, the governing equations are nondimensionalized by a reference length defined as $l_0 = \sqrt{\sigma/g(\rho_l - \rho_v)}$ and a reference time as $t_0 = \sqrt{l_0/g}$. The following parameters, which are evaluated from the properties of saturated water at 1 atm, are used for all of the computations presented in this article:

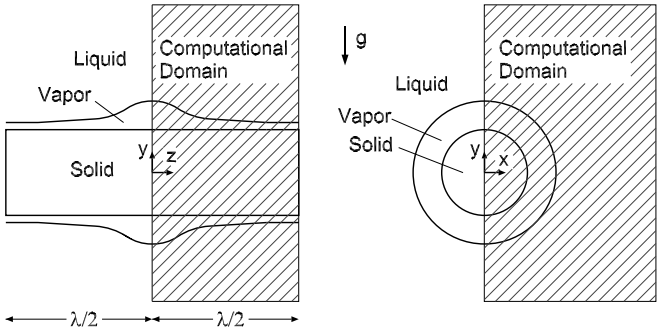

Fig. 1. Computational domain.

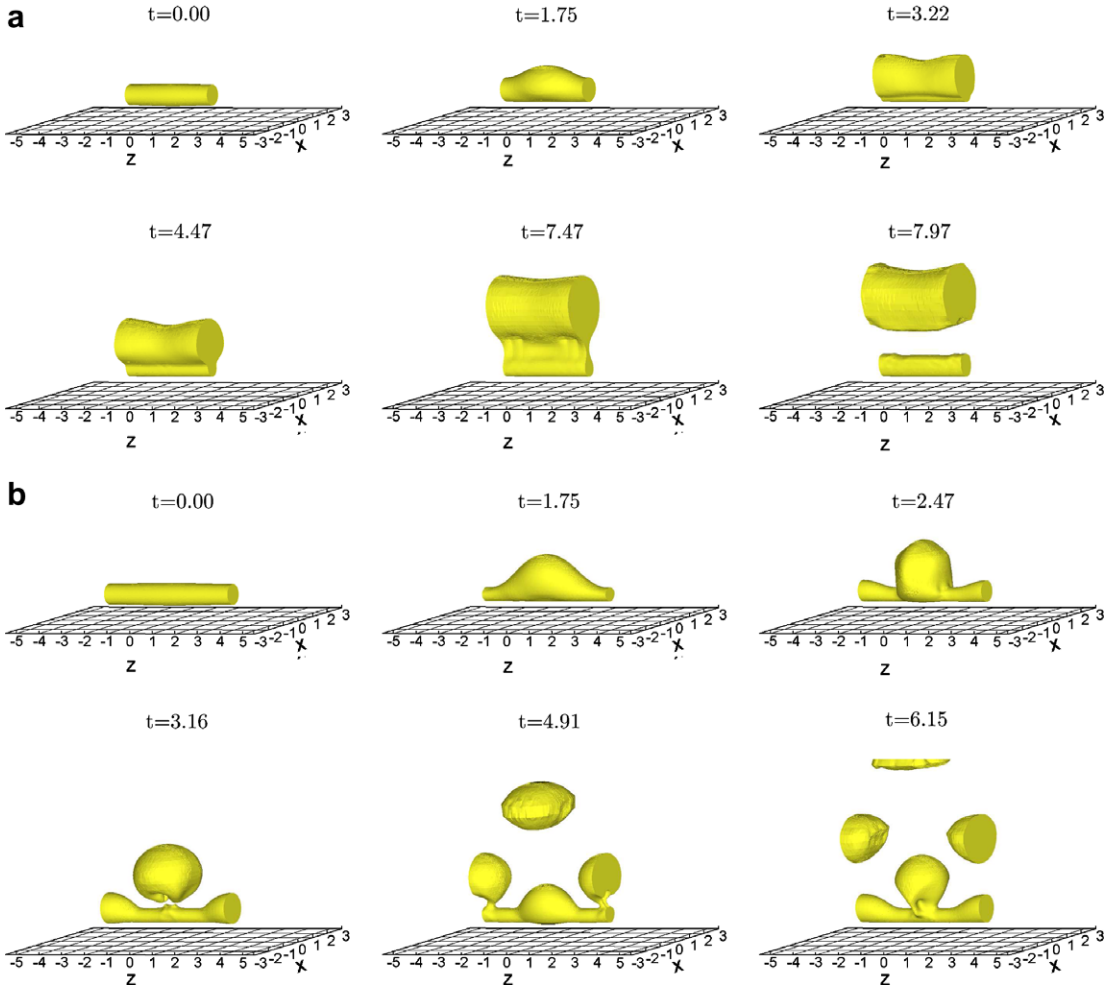

Fig. 2. Evolution of the liquid–vapor interface for different wavelengths at $\widehat{D} = 0.5$ and $g = 1g_e$: (a) $\lambda = 0.33\lambda_{dF}$, (b) $\lambda = 0.5\lambda_{dF}$, (c) $\lambda = 0.67\lambda_{dF}$, and (d) $\lambda = \lambda_{dF}$.

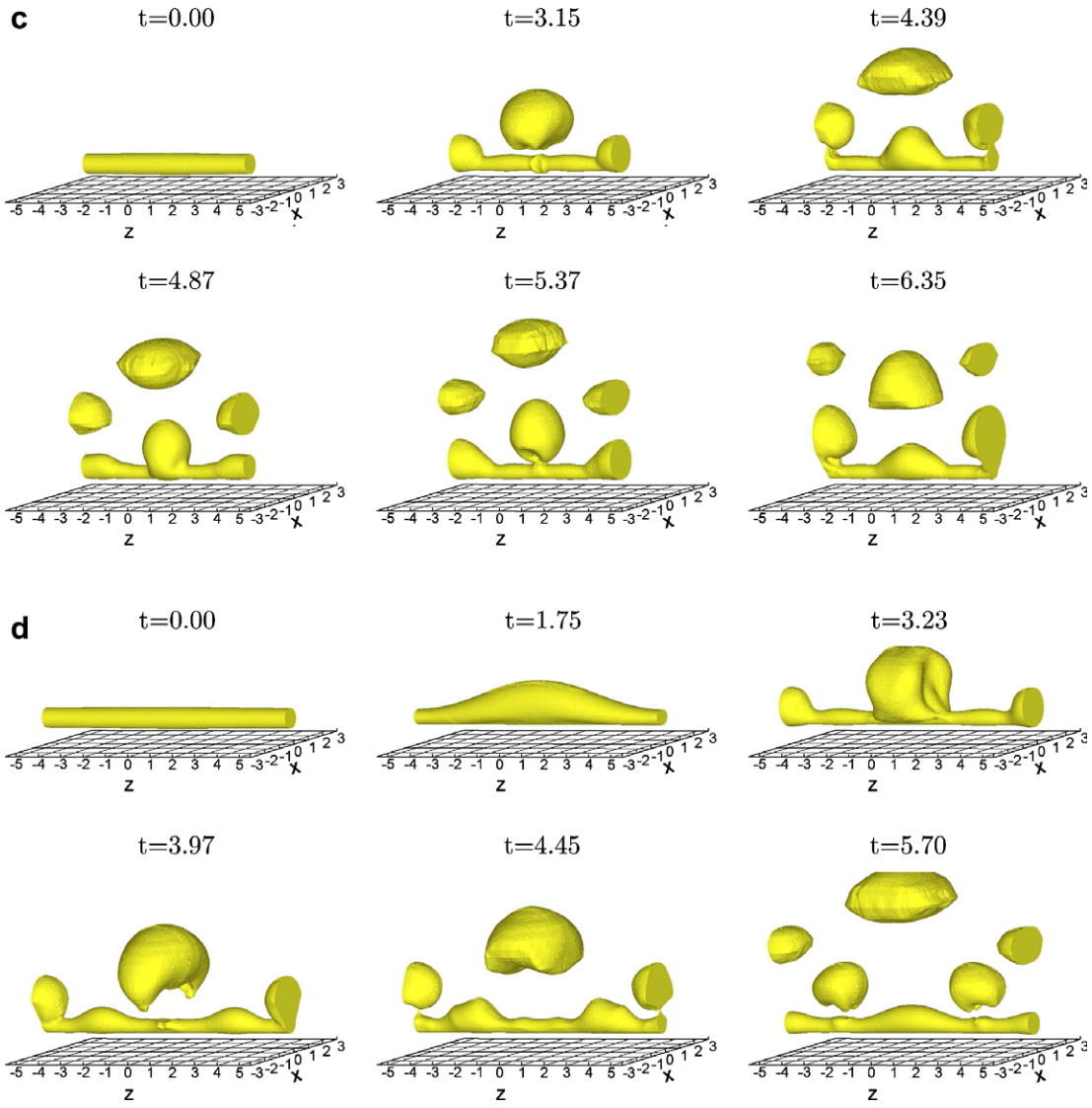

Fig. 2 (*continued*)

$$\frac{\rho_v}{\rho_l} = 6.24 \times 10^{-4}, \quad \frac{\mu_v}{\mu_l} = 4.26 \times 10^{-2}, \quad l_0\sqrt{\frac{g}{g_e}} = 2.5 \text{ mm}$$

$$\frac{Gr}{\hat{D}^3}\sqrt{\frac{g}{g_e}} = 6.01 \times 10^5, \quad Pr_v = 0.99, \quad Ja = 0.18$$

(for $T_w - T_{sat} = 200\ ^\circ\text{C}$)

The fluid properties including density, viscosity, specific heat and thermal conductivity are assumed to be constant in each phase. The temperature dependence of vapor properties can play a role for film boiling, but it is not included in the present study. This is not so restrictive when the heat transfer coefficients predicted numerically are compared with those obtained from correlations using the properties evaluated at the same temperature. If the reference temperature for evaluation of vapor properties is increased by 100 °C, ρ_v is reduced by 23%, c_v is increased by 33% and μ_v is increased by 34%. Using the vapor properties for $\hat{D} = 0.5$ and $g = 1g_e$, the heat transfer coefficient is increased by 13% in the present analysis and by 10% in the prediction from Sakurai et al. [3]. The effect of radiation on film boiling also was checked, as done in our previous work [7]. Its contribution to the heat transfer coefficient is less than 6.5% in all cases investigated in this work when using the assumed radiative emissivity of 0.5. Therefore, as long as the wall superheat is not very high, the radiation effect can be neglected.

In film boiling on a cylinder, the most dangerous wavelength which varies with the vapor layer thickness can not be predetermined but should be obtained as part of solutions. As such the computations were carried out for various wavelengths. Fig. 2 shows evolution patterns of the liquid–vapor interface for different wavelengths at $\hat{D} = 0.5$ and $g = 1g_e$. The computational domain is taken to be a region of $|x| \leqslant 3.3$, $-3.6 \leqslant y \leqslant 11.5$ and $|z| \leqslant 0.5\lambda$. The fluid and solid regions are represented by the LS function, $\psi = \sqrt{x^2 + y^2} - 0.25$. To save computational time, we use non-uniform meshes with the ratio of two adjacent

intervals of 1.1 except near the cylinder surface, $|x| \leqslant 0.3$ and $|y| \leqslant 0.3$, where the grid spacing is uniform as 0.01. The grid spacing in the z direction is chosen as 0.057. Initially the interface is disturbed sinusoidally as $\phi = \sqrt{x^2+y^2} - [0.4 + 0.015\cos(2\pi z/\lambda)]$. The vapor temperature profile is taken to be linear and fluid velocity is set to be zero. It is found from Fig. 2a that for $\lambda = 0.33\lambda_{dF}$, which corresponds the most dangerous wavelength predicted from Lienhard and Wong's equation (4), the formation and release of a bubble occurs in a nearly two-dimensional pattern. During the early period, the growth of the interface in the peak region at $z = 0$ is much faster than in the valley region at $|z| = 0.5\lambda$. However, for $t \geqslant 1.75$, the z-direction variation (or disturbance) of the interface is not further developed. This inconsistency with the prediction of Lienhard and Wong can be explained by noting that the diameter of the computed interface, $\widehat{D}_I$, is much larger than the cylinder diameter, $\widehat{D}$, in contrast to the assumption, $\widehat{D}_I \simeq \widehat{D}$, used in the analysis of Lienhard and Wong. When $\widehat{D}_I \geqslant 2\widehat{D}$, as seen at $t = 1.75$, the critical wavelength, which can be obtained from $\lambda_c = \lambda_d/\sqrt{3}$ and Eq. (5), is larger than $0.33\lambda_{dF}$. When the wavelength is increased to $\lambda = 0.5\lambda_{dF}$, the evolution of the interface occurs in a three-dimensional pattern, as demonstrated in Fig. 2b. Discrete vapor bubbles are released alternatively at the node, $z = 0$, and antinodes, $|z| = 0.5\lambda$, of the upper portion of the cylinder. A similar evolution pattern of the interface is observed in Fig. 2(c) for $\lambda = 0.67\lambda_{dF}$. The period of bubble release measured at $z = 0$ is $2.22t_0$, which is much smaller than the period of $2.99t_0$ for $\lambda = 0.5\lambda_{dF}$. This means that the most unstable wavelength (or the most probable bubble spacing) is closer to $0.67\lambda_{dF}$ than $\lambda = 0.5\lambda_{dF}$. As λ is further increased to λ_{dF}, which is the most unstable wavelength for film boiling on a flat plate, the bubble are released at more locations, as shown in Fig. 2d. During the early period, vapor bubbles are released alternatively at $z = 0$ and $|z| = 0.5\lambda$. However, after $t = 5.7$, bubble release also occurs at $|z| = 0.3\lambda$. This indicates that the most dangerous wavelength for film boiling shrinks on a small-diameter cylinder, as experimentally observed in [5,6].

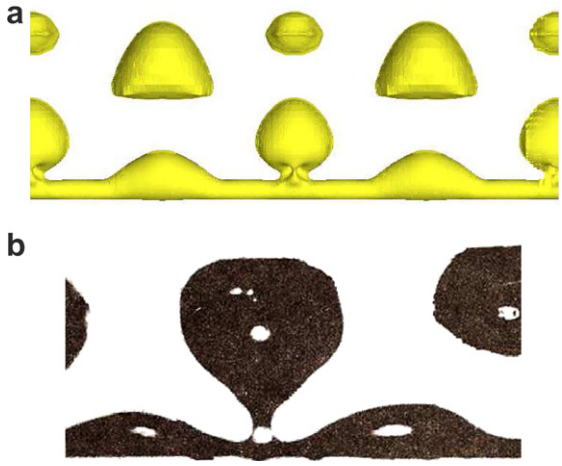

Fig. 3. Comparison of interface shapes during film boiling: (a) numerical simulation for water at $\widehat{D} = 0.5$ and $\lambda = 0.67\lambda_{dF}$ and (b) experiment for cyclohexanol at $\widehat{D} = 0.46$ and $\lambda = 0.70\lambda_{dF}$.

The interface shape predicted from the numerical simulation for $\lambda = 0.67\lambda_{dF}$ is compared in Fig. 3 with that observed in the experiments [22] for film boiling of cyclohexanol at $\widehat{D} = 0.46$ and $\lambda = 0.70\lambda_{dF}$. It is seen that bubble release pattern calculated numerically is in agreement with that obtained experimentally except that the computed bubble at departure is smaller than observed in the experiment. This is possibly caused by the fact the vapor volume flux per the surface area of cylinder, $\dot{V}_v$, obtained under the computational condition is much smaller than the experimental condition: $\dot{V}_v = 4.25 \times 10^{-2}\ m^3/m^2\ s$ in the computation whereas $\dot{V}_v = 13.8\ m^3/m^2\ s$ in the experiment. Increased vapor volume flux in the experiments is associ-

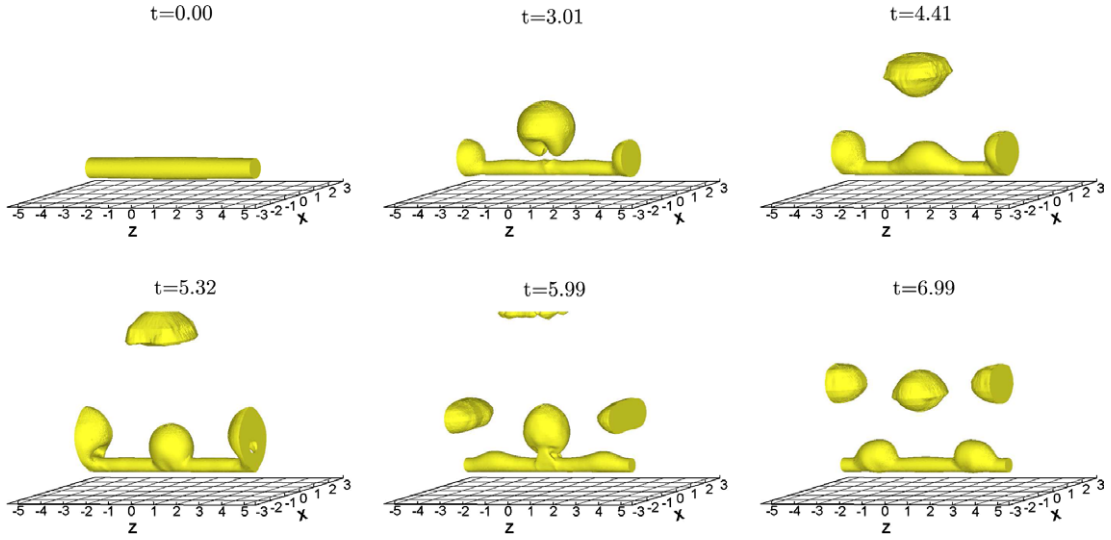

Fig. 4. Evolution of the liquid–vapor interface for $\widehat{D} = 0.5$, $g = 0.01g_e$ and $\lambda = 0.67\lambda_{dF}$.

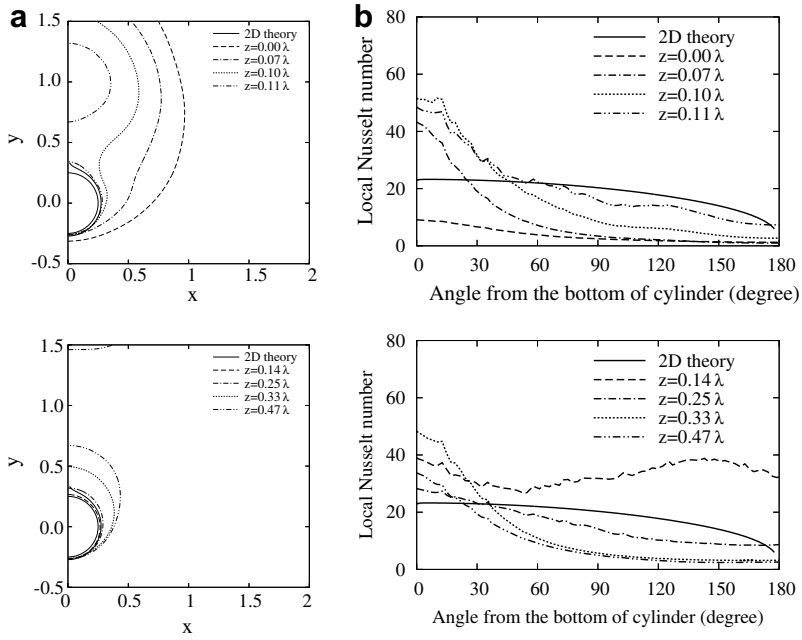

Fig. 5. Results at $t = 4.87$ for $\widehat{D} = 0.5, g = 1\ g_e$ and $\lambda = 0.67\lambda_{dF}$: (a) interface shape and (b) local Nusselt number.

ated with the much reduced vapor density at the low pressures (about 1 kPa) in comparison to that used in the analysis. The simulation for the condition of the experiment is possible without any change in the present numerical method, but it requires quite a large computational domain to accommodate the departing bubbles which become larger with the increase in vapor volume flux at very low pressure.

Fig. 4 shows the evolution pattern of the interface at low gravity, $g = 0.01g_e$, while keeping $\widehat{D} = 0.5$ and $\lambda = 0.67\lambda_{dF}$. After the first cycle of bubble release occurs alternatively at the node and antinodes, the bubble spacing is found to shrink at $t = 6.99$. This reduction in the bubble spacing (or the dominant wavelength) can be explained from Eq. (5), in which λ_d/λ_{dF} decreases as the vapor bulge or the departing bubble becomes much smaller with the reduction of gravity.

The spatial variation of the interface position and Nusselt number on different positions in the z direction for $\widehat{D} = 0.5, g = 1g_e$ and $\lambda = 0.67\lambda_{dF}$ is plotted in Fig. 5 after a quasi-steady state condition has been achieved. The Nusselt number is defined as $Nu = Dq_w/k_v(T_w - T_{sat})$. It is seen that most of heat is transferred via the thin film on the lower portion of the cylinder. The heat flux on the upper portion is very small except near $z = 0.14\lambda$, which corresponds to the valley of interfacial wave formed on the upper portion of the cylinder. The circumferential variations of vapor film thickness and local Nusselt number obtained from numerical simulation are quite different from the theoretical predictions of Bromley [1], which does not include the effect of interfacial wave in the z direction. The Nusselt numbers based on the wall heat flux averaged over the surface area of cylinder are plotted in Fig. 6. It is

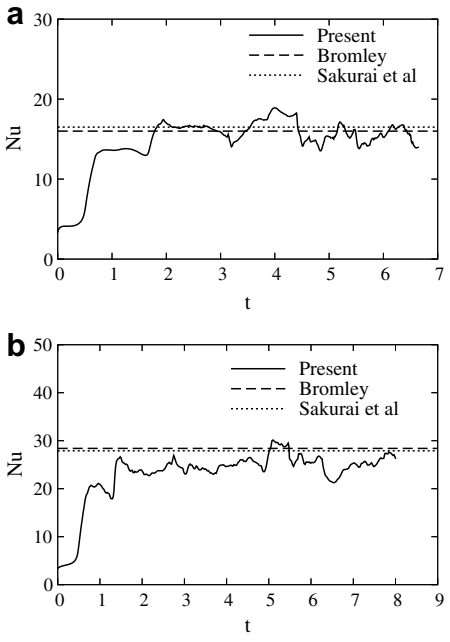

Fig. 6. Variation of Nusselt number with time for $\widehat{D} = 0.5$ and $\lambda = 0.67\lambda_{dF}$ and different gravities: (a) $g = 1g_e$ and (b) $g = 0.01g_e$.

observed that the heat transfer coefficient varies in time, depending on the interfacial motion. After the bubble pinches off, the heat transfer coefficient increases as the vapor bulge on the top portion of the cylinder grows, which results in the increase of the buoyancy force that pulls up and hence thins the vapor film surrounding the cylinder. The heat transfer coefficient drops during the bubble pinch-off process in which the surface tension force dominant over the buoyancy force restores the disturbed inter-

face. The Nusselt number is found to increase when the gravity is reduced while keeping $\widehat{D}$ constant. It is also noted that the Nusselt number varies slightly in time except during the early period when the heat transfer is affected by the artificially specified initial condition. The calculations were not carried out until the initial transients disappear completely and the results clearly demonstrate the quasi-steady cyclic behavior, which requires tremendous computational time for three-dimensional simulation of film boiling. The Nusselt numbers averaged over the computational period except the first cycle of bubble release are listed in Table 1. This values are in good agreement with those predicted from the correlations of Bromley [1], Breen and Westwater [2] and Sakurai et al. [3]. For $\widehat{D} = 0.5$, the dependence of Nusselt numbers obtained from the present work on gravity can be expressed as $Nu/Nu_e = (g/g_e)^{-0.108}$. This is comparable with $Nu/Nu_e = (g/g_e)^{-0.125}$ and $(g/g_e)^{-0.115}$, which are obtained from the correlations given in [1,2] and [3], respectively.

Table 1
Predicted Nusselt numbers

	$g = 1g_e$			$g = 0.01g_e$	
D (mm)	0.125	1.25	12.5	1.25	12.5
D/l_0	0.05	0.5	5	0.05	0.5
Bromley [1]	2.84	16.0	90.0	5.05	28.4
Breen and Westwater [2]	12.7	20.0	92.6	22.5	35.5
Sakurai et al. [3]	5.57	16.4	89.0	8.93	27.9
Present work	5.40	15.4	96.2	9.37	25.3

Fig. 7 presents the evolution pattern of the interface during film boiling on a fine wire, $\widehat{D} = 0.05$. The computation is made in a domain of $|x| \leqslant 3.3$, $-1.6 \leqslant y \leqslant 11.5$ and $|z| \leqslant 0.5\lambda$. Uniform meshes with $h = 0.002$ are used near the cylinder, $|x| \leqslant 0.032$ and $|y| \leqslant 0.032$, whereas non-uniform meshes are used for the other region. The grid spacing in the z direction is 0.012. The wavelength is chosen as $\lambda = 0.14\lambda_{dF}$ from several preliminary computations. For a smaller wavelength, say, $\lambda = 0.07\lambda_{dF}$, which is twice the most dangerous wavelength predicted from Lienhard and Wong's equation (4), the evolution of the interface occurs in a two-dimensional pattern, as observed in Fig. 2a. Compared with the result for $\widehat{D} = 0.5$, Fig. 7 shows quite different interface configurations. The vapor layer grows axisymmetrically around the cylinder during the whole period except while bubbles depart, which indicates the surface tension force is dominant over the buoyancy force during most of period of film boiling on a fine wire. While the bubbles are released alternatively at the node, $z = 0$, and at the antinodes, $|z| = 0.5\lambda$, the small vapor bulges (or bubbles) are observed to form frequently at $|z| = 0.25\lambda$. The small bubbles merge into the bubbles at the node or antinodes

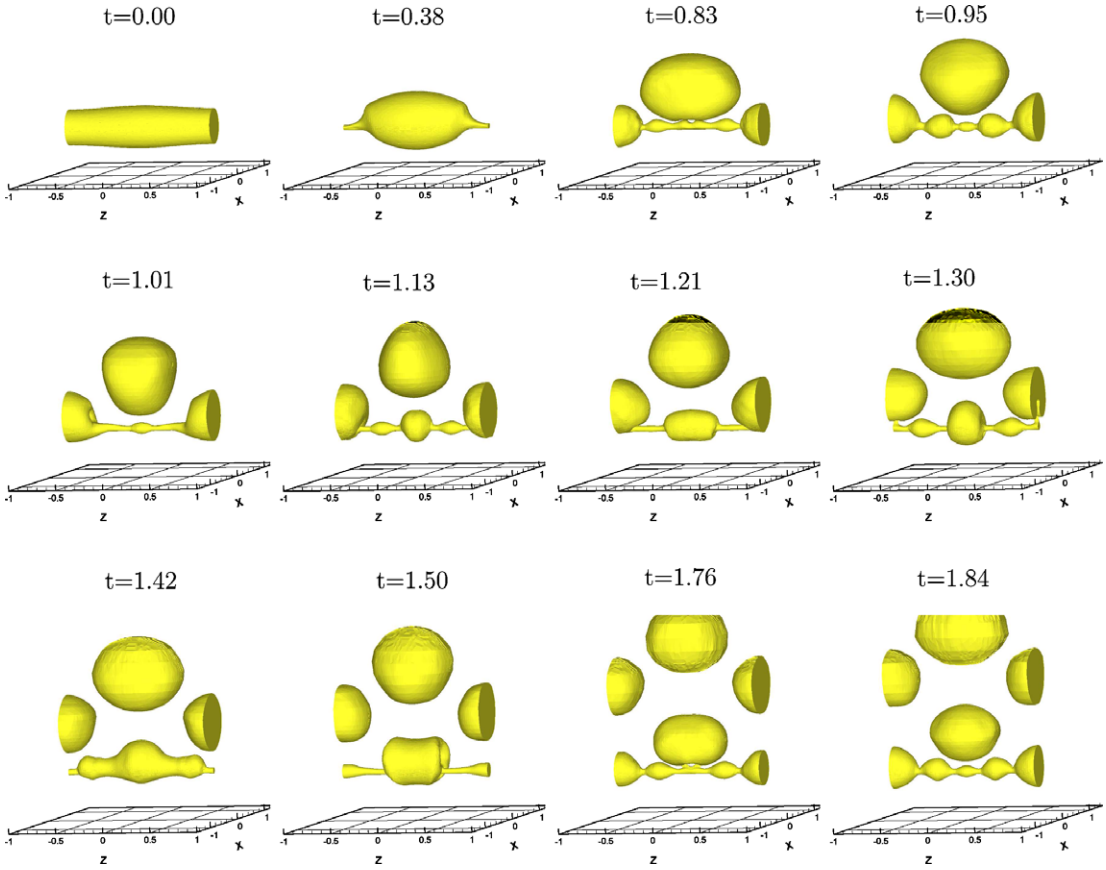

Fig. 7. Evolution of the liquid–vapor interface at $\widehat{D} = 0.05$, $g = 1g_e$ and $\lambda = 0.14\lambda_{dF}$.

rather than they grow up to departing bubbles. This bubble merger pattern, as mentioned by Lienhard and Sun [6], is one of the main features occurring in the bubble departure (or vapor removal) process of film boiling on a fine wire, which requires a large vapor volume to overcome the strong surface tension force holding the bubbles on the wire. When the gravity is reduced to $g = 0.01g_e$, while keeping $\widehat{D} = 0.05$ and $\lambda = 0.14\lambda_{dF}$, the evolution pattern of the interface is quite similar except that the dimensionless bubble diameter at departure becomes smaller, as demonstrated in Fig. 8. This indicates that the interfacial motion on a fine wire is little affected by the gravity as long as dimensionless wire diameter is held constant.

Fig. 9 shows the Nusselt number for $\widehat{D} = 0.05$. Unlike the results for $\widehat{D} = 0.5$, the temporal variation of Nusselt numbers is quite large, which is reflective of frequently occurring bubble mergers. Also, the Nusselt number is observed to become larger under the reduced gravity condition. The time averaged Nusselt numbers are listed in Table 1. The Nusselt numbers obtained from the present analysis match much better with those predicted from the correlation of Sakurai et al. than predicted from the other two correlations. For $\widehat{D} = 0.05$, the dependence of Nusselt numbers obtained numerically on gravity can be expressed as $Nu/Nu_e = (g/g_e)^{-0.120}$, which is comparable with the predictions from the correlations [1–3], $Nu/Nu_e = (g/g_e)^{-0.125}$ and $(g/g_e)^{-0.102}$. For a given dimensionless cylinder diameter, $\widehat{D}$, the numerical simulation as well as the empirical correlations consistently show that the Nusselt number increases weakly with the reduction of gravity. However,

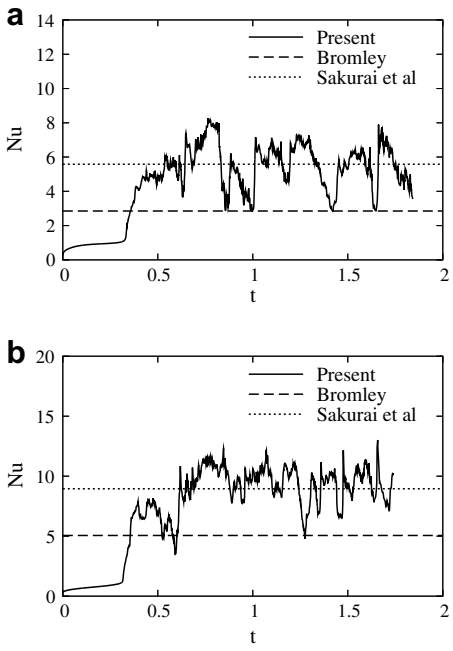

Fig. 9. Variation of Nusselt number with time for $\widehat{D} = 0.05$ and $\lambda = 0.14\lambda_{dF}$ and different gravities: (a) $g = 1g_e$ and (b) $g = 0.01g_e$.

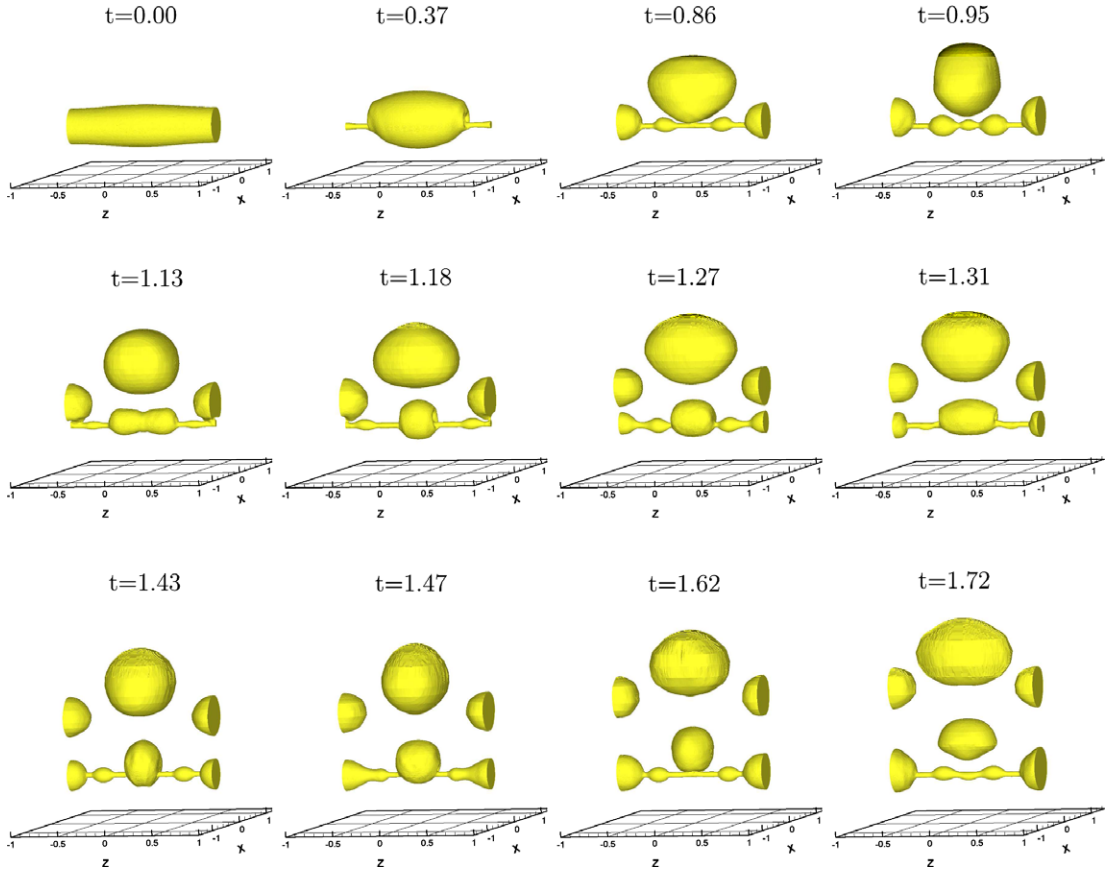

Fig. 8. Evolution of the liquid–vapor interface at $\widehat{D} = 0.05$, $g = 0.01g_e$ and $\lambda = 0.14\lambda_{dF}$.

while fixing D rather than $\widehat{D}$, the effect of gravity on Nusselt number obtained from the present work is more pronounced as seen from the expressions, $Nu/Nu_e = (g/g_e)^{0.108}$ for $D = 1.25$ mm and $Nu/Nu_e = (g/g_e)^{0.290}$ for $D = 12.5$ mm. It is noted from Table 1 that for a given cylinder diameter the Nusselt number decreases as the gravity is reduced in all cases except prediction from Breen and Westwater's correlation for $D = 1.25$ mm.

The evolution pattern of the interface during film boiling on a large cylinder, $\widehat{D} = 5$, is plotted in Fig. 10. The computational domain is taken to be a region of $|x| \leqslant 5.6$, $-4.1 \leqslant y \leqslant 11.5$ and $|z| \leqslant 0.5\lambda_{dF}$. Uniform meshes with $h = 0.04$ are used near the cylinder, $|x| \leqslant 2.6$ and $|y| \leqslant 2.6$, whereas non-uniform meshes are used for the other region. The grid spacing in the z direction is 0.17. In contrast to the results for small-diameter cylinders, where the bubble release occurs only on the top of the cylinder, the result for $\widehat{D} = 5$ shows the interfacial disturbance grows in a two-dimensional wave pattern along the upper portion of the cylinder, as seen at $t = 1.75$ and $t = 4.23$ and then the bubbles are released at various circumferential positions. This bubble release pattern for film boiling on a large cylinder is consistent with the experimental observation of Breen and Westwater [2].

The effect of dimensionless cylinder diameter, $\widehat{D}$ or D/l_0, on the most dangerous wavelength and Nusselt number is shown in Fig. 11. It is seen that for small value of $\widehat{D}$ the most dangerous wavelengths obtained from the present numerical study as well as Lienhard and Sun's experimen-

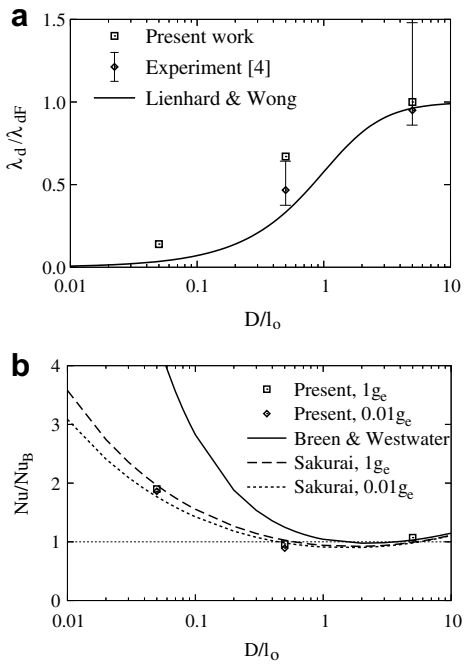

Fig. 11. Effect of dimensionless cylinder diameter, D/l_0, on (a) the most dangerous wavelength and (b) Nusselt number.

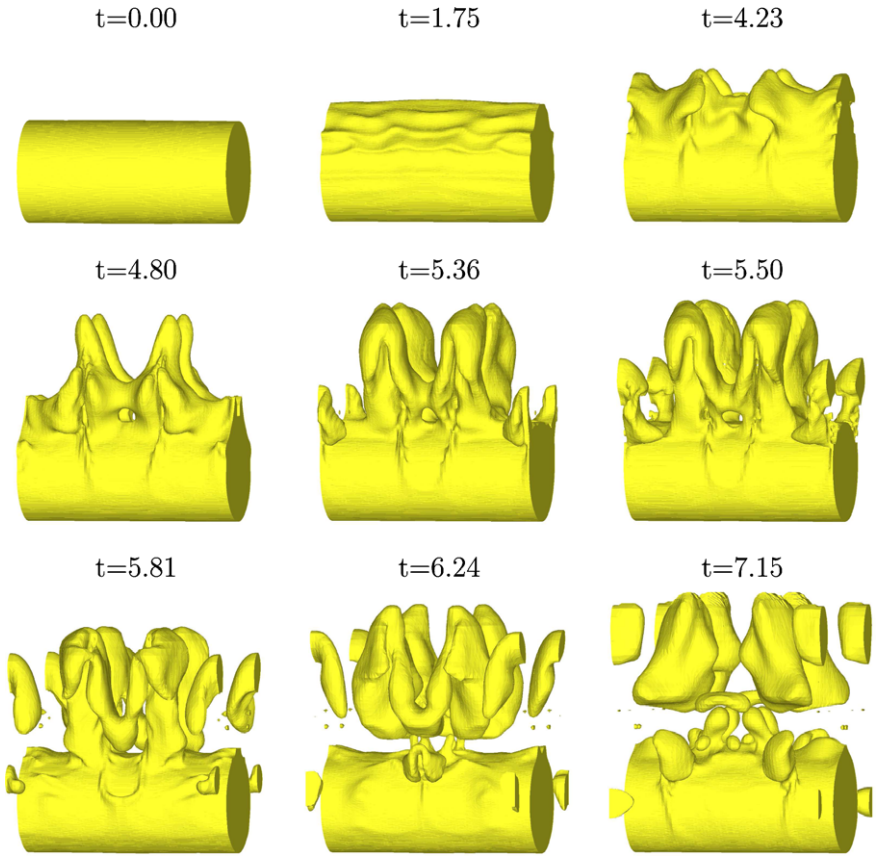

Fig. 10. Evolution of the liquid–vapor interface at $\widehat{D} = 5, g = 1g_e$ and $\lambda = \lambda_{dF}$.

tal study [6] are larger than those predicted from Lienhard and Wong's equation (4). The most dangerous wavelength is determined by not only the cylinder diameter but also the vapor layer thickness on the upper portion of the cylinder, as discussed by Dhir and Lienhard [23]. If the vapor film thickness is included in Lienhard and Wong's equation, its prediction for the most dangerous wavelength will be closer to the numerical result. In Fig. 11b, the Nusselt numbers obtained from the present analysis are compared with those predicted from the correlations of Bromley [1], Breen and Westwater [2] and Sakurai et al. [3]. The present results match within at most $\pm 10\%$ deviation with Sakurai et al.'s predictions.

4. Conclusions

1. Three-dimensional simulations of saturated film boiling on a horizontal cylinder have been performed successfully.
2. Based on the numerical simulation, it is shown that during film boiling on small-diameter cylinders discrete vapor bubbles are released only on the top portion of the cylinder. With further decrease in cylinder diameter the bubble merger pattern also appears as part of the vapor removal process whereas with increase in cylinder diameter bubbles are released at various circumferential positions in a two-dimensional wave pattern. This is consistent with visual observations reported in the literature.
3. The most dangerous wavelength in film boiling on a horizontal cylinder decreases with cylinder diameter. The dominant wavelength is determined by the diameter of surrounding interface, which can be much larger than the cylinder diameter in case of a small cylinder.
4. The Nusselt numbers obtained from the present analysis compare within at most $\pm 10\%$ deviation with those predicted from Sakurai et al.'s correlation.

Acknowledgement

This work received support from NASA Microgravity Fluid Physics program.

References

[1] L.A. Bromley, Heat transfer in stable film boiling, Chem. Eng. Progr. 46 (1950) 221–227.
[2] B.P. Breen, J.W. Westwater, Effect of diameter of horizontal tubes on film boiling heat transfer, Chem. Eng. Progr. 58 (1962) 67–72.
[3] A. Sakurai, M. Shiotsu, K. Hata, A general correlation for pool film boiling heat transfer from a horizontal cylinder to subcooled liquid. Part 2: experimental data for various liquids and its correlation, J. Heat Transfer 112 (1990) 441–450.
[4] S. Nishio, H. Ohtake, Vapor-film-unit model and heat transfer correlation for natural-convection film boiling with wave motion under subcooled conditions, Int. J. Heat Mass Transfer 36 (1993) 2541–2552.
[5] J.H. Lienhard, P.T.Y. Wong, The dominant unstable wavelength and minimum heat flux during film boiling on a horizontal cylinder, J. Heat Transfer 86 (1964) 220–226.
[6] J.H. Lienhard, K.H. Sun, Effects of gravity and size upon film boiling from horizontal cylinders, J. Heat Transfer 92 (1970) 292–298.
[7] G. Son, V.K. Dhir, Numerical simulation of saturated film boiling on a horizontal surface, J. Heat Transfer 119 (1997) 525–533.
[8] D. Juric, G. Tryggvason, Computations of boiling flows, Int. J. Multiphase Flow 24 (1998) 387–410.
[9] G. Son, V.K. Dhir, Numerical simulation of film boiling near critical pressures with a level set method, J. Heat Transfer 120 (1998) 183–192.
[10] S.W.J. Welch, J. Wilson, A volume of fluid based method for fluid flows with phase change, J. Comput. Phys. 160 (2000) 662–682.
[11] A. Esmaeeli, G. Tryggvason, A front tracking method for computations of boiling in complex geometries, Int. J. Multiphase Flow 30 (2004) 1037–1050.
[12] N. Al-Rawahi, G. Tryggvason, Numerical simulation of dendritic solidification with convection: two-dimensional geometry, J. Comput. Phys. 180 (2002) 471–496.
[13] G. Son, V.K. Dhir, A level set method for analysis of film boiling on an immersed solid surface, Numer. Heat Transfer, Part B 52 (2007) 153–177.
[14] D.Q. Nguyen, R.P. Fedkiw, M. Kang, A boundary condition capturing method for incompressible flame discontinuities, J. Comput. Phys. 172 (2001) 71–98.
[15] R.P. Fedkiw, T. Aslam, B. Merriman, S. Osher, A non-oscillatory Eulerian ap proach to interfaces in multimaterial flows (the ghost fluid method), J. Comput. Phys. 152 (1999) 457–492.
[16] M. Kang, R.P. Fedkiw, X.-D. Liu, A boundary condition capturing method for multiphase incompressible flow, J. Sci. Comput. 15 (2000) 323–360.
[17] F. Gibou, R.P. Fedkiw, L.-T. Cheng, M. Kang, A second-order-accurate symmetric discretization of the Poisson equation on irregular domains, J. Comput. Phys. 176 (2002) 205–227.
[18] S. Marella, S. Krishnan, H. Liu, H.S. Udaykumar, Sharp interface Cartesian grid method I: an easily implemented technique for 3D moving boundary com putations, J. Comput. Phys. 210 (2005) 1–31.
[19] M. Sussman, K.M. Smith, M.Y. Hussaini, M. Ohta, R. Zhi-Wei, A sharp in terface method for incompressible two-phase flows, J. Comput. Phys. 221 (2007) 469–505.
[20] M. Sussman, P. Smereka, S. Osher, A level set approach for computing solutions to incompressible two-phase flow, J. Comput. Phys. 114 (1994) 146–159.
[21] G. Son, A level set method for two-fluid flows with immersed solid boundaries, Numer. Heat Transfer, Part B 47 (2005) 473–489.
[22] J.H. Lienhard, V.K. Dhir, Extended hydrodynamic theory of the peak and minimum pool boiling heat fluxes, NASA CR-2270, 1973.
[23] V.K. Dhir, J.H. Lienhard, Taylor stability of viscous fluids with application to film boiling, Int. J. Heat Mass Transfer 16 (1973) 2097–2109.